Effects of Surface Drag on Fronts within Numerically Simulated Baroclinic Waves

RICHARD ROTUNNO, WILLIAM C. SKAMAROCK, AND CHRIS SNYDER

National Center for Atmospheric Research, Boulder, Colorado*

(Manuscript received 18 April 1997, in final form 5 November 1997)

ABSTRACT

A comparative analysis of simulations of baroclinic waves with and without surface drag is presented, with particular reference to surface features. As in recent studies, the present simulations show that, compared to simulations with no drag, those with surface drag are less inclined to develop a secluded warm sector, and that drag weakens the warm front while the cold front remains strong. The authors demonstrate that analogous effects occur when Ekman pumping is used in nonlinear quasigeostrophic numerical simulations of unstable baroclinic waves in a channel. However, since the quasigeostrophic model produces symmetric highs and lows in the unstable baroclinic wave, the cold and warm fronts are therefore also symmetric and hence equally affected by the Ekman pumping. The different effect that friction has on the warm front with respect to the cold front in the primitive-equation simulations is fundamentally related to the tendency for the lows to be strong and narrow and the highs weak and broad, and for the warm front to form just north of, and extend eastward from, the low, while the cold front extends between the high and the low. The authors' thesis is that the Ekman pumping associated with the low, at the location where the warm front would form in the absence of surface friction, acts to resist the formation of the warm front, while the cold front, positioned between the high and the low where Ekman pumping associated with the baroclinic wave is weak, is therefore relatively unaffected.

Given the weakness of Ekman pumping associated with the baroclinic wave in the vicinity of the incipient cold front, the present simulations indicate that cold frontogenesis occurs in the drag case in much the same way as in the no-drag case. Present analysis shows that the horizontal advection creating the cold front is a combination of geostrophic and ageostrophic effects. A portion of the ageostrophic frontogenesis is a response to geostrophic frontogenesis, as in the case without surface drag; however with surface drag, a significant portion of the cross-front ageostrophic flow is due to the Ekman layer associated with the front itself.

1. Introduction

Theoretical and numerical studies of frontogenesis within baroclinic waves have focused largely on the ''no-drag'' idealization. In a recent addition to this line, the present authors (Rotunno et al. 1994, hereafter RSS) analyzed the frontogenesis that occurs within numerically simulated baroclinic waves. Using the same zonal jet with a stratosphere as in RSS, we present here a comparative analysis of simulations of baroclinic waves with and without surface drag.

As in recent studies, the present simulations show that, compared to simulations with no drag, those with surface drag are less inclined to develop a secluded warm sector (Kuo and Low-Nam 1994) and that drag weakens the warm front while the cold front remains strong (Hines and Mechoso 1993).

Kuo and Low-Nam (1994) showed that in their simulations with drag, warm-sector air is Ekman pumped out of the boundary layer, and so it is more difficult to form a long tongue of warm air at the surface and hence harder to ''seclude'' it. Analysis of the present primitive-equation (PE) simulations supports this finding; moreover, we show that this same effect occurs in simple nonlinear quasigeostrophic (QG) numerical simulations of unstable baroclinic waves in a channel. However, since the QG model produces symmetric highs and lows in the unstable baroclinic wave, the cold and warm fronts are therefore also symmetric and hence equally affected by the Ekman pumping. The different effect that friction has on the warm front with respect to the cold front in the PE simulations is thus fundamentally related to the tendency in those simulations, as shown in Snyder et al. (1991, hereafter SSR), for the lows to be strong and narrow, the highs weak and broad, and for the warm front to form just north of, and extend eastward from, the low, while the cold front extends in an arc between the high and the low (see Fig. 4 of SSR). Our thesis is that the Ekman pumping associated with the low, at the location where the warm front would form in the absence of surface friction, acts to resist the formation of the warm front, while the cold front, po-

* The National Center for Atmospheric Research is sponsored by the National Science Foundation.

Corresponding author address: Dr. Richard Rotunno, NCAR/MMM Division, P.O. Box 3000, Boulder, CO 80307.
E-mail: rotunno@ncar.ucar.edu

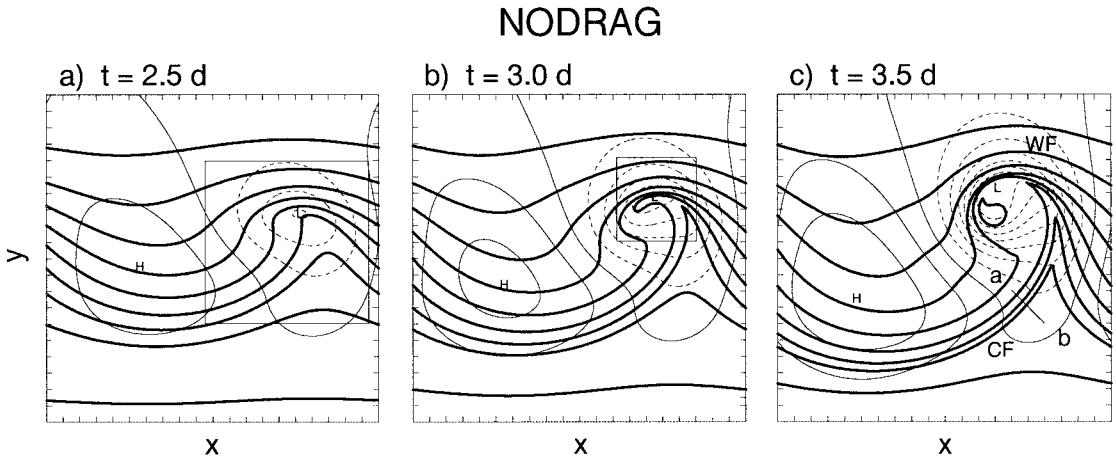

FIG. 1. Potential temperature θ (heavy lines, contour interval = 5 K) and geopotential ϕ (thin lines, contour interval = 500 m^2 s^{-1}, roughly 5 mb) at t = (a) 2.5, (b) 3.0, and (c) 3.5 d at z = 500 m from the numerical simulations without surface drag. The zero line in the ϕ field is the first solid contour line; dashed lines indicate negative values. A full wavelength (4000 km) in the zonal direction, and a 4000-km portion of the 8000-km domain in meridional direction, is shown. Tick marks indicate 200-km intervals. The box in (a) indicates the analysis domain shown in Fig. 5, and the box in (b) is the analysis domain for the NODRAG part of Fig. 9. In (c), the line a–b indicates a section for the analysis shown in Fig. 6. Here and subsequently, CF and WF are placed in the proximity of the cold and warm front, respectively. The L denotes the position of the low pressure center.

sitioned between the high and the low, at the location where Ekman pumping associated with the baroclinic wave is weak, is therefore relatively unaffected.

Given the weakness of Ekman pumping associated with the baroclinic wave in the vicinity of the incipient cold front, the present simulations indicate that cold frontogenesis occurs in the drag case in much the same way as in the no-drag case: Horizontal advection of cold air toward more slowly moving warm air is the proximate cause. Further analysis shows that the horizontal advection creating the cold front is a combination of geostrophic and ageostrophic effects. A portion of the ageostrophic flow is an inviscid response to the geostrophic frontogenesis, along the lines of the model introduced by Hoskins and Bretherton (1972), but a significant portion of the cross-front ageostrophic velocity is due to the Ekman layer associated with the front itself.

A new feature of the present high-resolution simulations is the formation of an intense, rotating updraft located at the tip of the warm tongue in the case with surface drag.

2. Numerical simulations with and without surface drag

Primitive-equation simulations of growing baroclinic waves on an f-plane Cartesian channel provide the testing ground for the effects of surface drag on frontogenesis. The case without surface drag, designated NODRAG, is that described in RSS (section 4) with the exception that NODRAG was done with a horizontal grid size of 16.7 km (reduced from the 100-km value used in RSS; the vertical grid size, 250 m, is the same) and (to facilitate comparison with the simulations having surface drag) with the vertical-diffusion terms $\nu\partial_{zz}\mathbf{u}$ and $\nu\partial_{zz}\theta$ (ν = 5 m^2 s^{-1}) added to the momentum and heat equations, respectively. The initial condition is the zonal jet shown in Fig. 11 of RSS together with the most unstable normal mode with the maximum meridional velocity amplitude set to 1.7 m s^{-1}.[1] Figure 1 shows a time sequence of the potential temperature θ and geopotential ϕ (pressure) fields at z = 500 m during frontogenesis in NODRAG. The pressure low is intense and narrow, while the high is broad and weak; associated with this pressure asymmetry is a cyclonic wrapping of the isotherms near the low; the warm front (near WF) is thus in close proximity to the low, while the cold front (CF) extends in an arc between the high and the low.

The simulation with surface drag, designated DRAG, is done with the same basic state as in NODRAG, except for the inclusion of a surface-drag condition. A representation of the latter that facilitates analysis yet retains the basic sensitivity is as follows. The surface stress is specified by the linearized drag law $\boldsymbol{\tau} = K\mathbf{u}$ (e.g., Bannon and Salem 1995 and references therein), where K = 0.03 m s^{-1} [roughly a land value of the drag coefficient (0.003) from the nonlinear drag law times a nominal surface wind (10 m s^{-1})]; as in the NODRAG case, the stress in the interior $\boldsymbol{\tau} = \nu\partial_z\mathbf{u}$ (with ν = 10 m^2 s^{-1}). At the upper boundary, $\boldsymbol{\tau}$ = 0. We also allow for the vertical diffusion of θ by adding the term $\nu\partial_{zz}\theta$ to the thermodynamic equation. At the upper boundary, zero

[1] In RSS this amplitude was set to 0.17 m s^{-1} but was mistakenly reported as 1.7 m s^{-1}; hence the time to reach an equivalent wave amplitude is shorter in the present study.

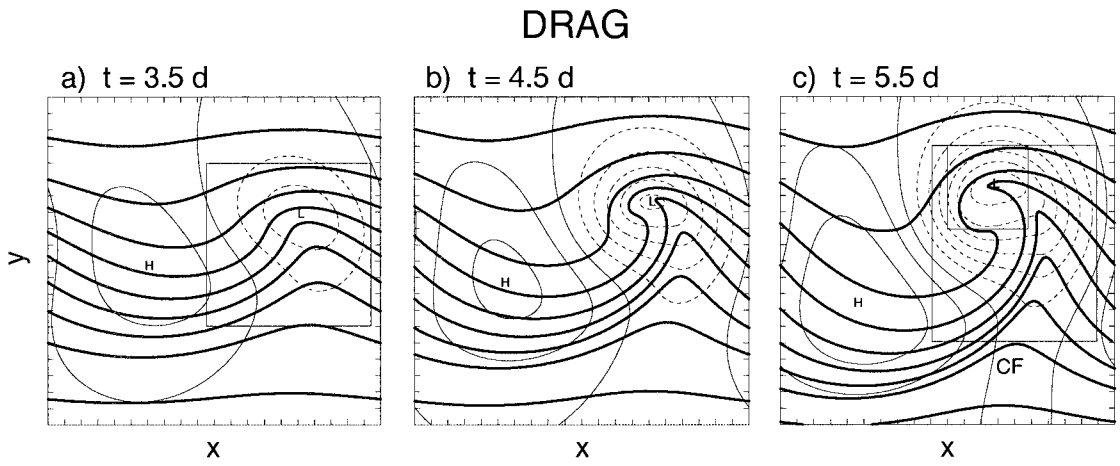

FIG. 2. Potential temperature θ and geopotential ϕ at $z = 500$ m at $t =$ (a) 3.5, (b) 4.5, and (c) 5.5 d from the numerical simulations with surface drag. Domain and plotting conventions as in Fig. 1. The box in (a) indicates the analysis domain shown in Fig. 4, the large box in (c) indicates the analysis domain for Fig. 7, and the small box in (c) indicates the analysis domain used in the DRAG part of Fig. 9.

heat flux is required ($\partial_z\theta = 0$). The lower boundary condition for θ requires further discussion.

Consistent with the level of idealization of the present numerical experiments, two possible lower boundary conditions on θ come to mind: (a) zero surface heat flux and (b) surface temperature specified as that of the initial condition. One of the main intentions of this study is to build a bridge to simpler, better understood models for the effect of the boundary layer on the development of baroclinic waves and attendant frontogenesis. In quasigeostrophic theory, the boundary layer acts to modify θ only through the Ekman-layer-induced vertical advection of the horizontally invariant reference-state potential temperature (Pedlosky 1987, section 6.6); hence, no information about any particular surface temperature distribution is communicated to the QG flow. Thus we were motivated to use the first condition for the present study. From a phenomenological point of view, one might view the first condition as one where the time constant for the adjustment of the surface temperature to the air temperature is small (e.g., under certain conditions over land), while the second condition represents situations where that time constant is large (e.g., over sea). The second condition was used in the recent numerical study by Thompson and Williams (1997) of maritime frontogenesis. Differences in some of the results between that study and the present one can be attributed to the different lower boundary condition on θ (section 3c).

Figure 2 shows a time sequence of θ and ϕ at $z =$ 500 m during frontogenesis in DRAG. Because of the smaller growth rate of the unstable mode with surface drag (e.g., Williams and Robinson 1974), the time sequence chosen for display in Fig. 2 begins later, and has a longer time interval between frames, than that of the NODRAG case shown in Fig. 1. In NODRAG (Fig. 1) there is a ''tongue'' of warm air that protrudes into the low and then is secluded; the warm front is on the northern periphery of the seclusion. In DRAG (Fig. 2), the warm tongue again protrudes into the low, but instead of continuing to curl into a seclusion, the tongue narrows to a point; warmer isotherms have their northward progress completely arrested. The temperature contrast around the northern periphery of the tongue in DRAG is weak. On the other hand, a cold front forms in both cases and is located in a roughly similar geostrophic deformation field between the low and high. The present relatively simple calculations capture the asymmetric effect that drag has on the warm front with respect to the cold front, as seen in the study on the sphere using a nonlinear drag law and a convective-adjustment boundary layer by Hines and Mechoso (1993); they also capture the effect that drag has in making it more difficult for warm-air seclusion, seen in the study based on a real case using a mesoscale numerical weather prediction model by Kuo and Low-Nam (1994).

3. Explanations

a. Effects of drag in QG simulations

In the absence of diabatic processes, frontogenesis occurs by advection of θ surfaces closer to one another; how this occurs in a baroclinic wave is described to a first approximation by QG theory. Figure 3a contains the nondimensional surface θ and ϕ from an integration of the nonlinear QG equations described in section 4 of Rotunno and Bao (1996, hereafter RB). Briefly, the initial condition is a zonally invariant base state (basically a QG approximation to the base state shown in Fig. 11 of RSS), together with a sinusoidal tropospheric perturbation. After an adjustment period [$\sim$6 nondimensional time units ($\sim$1 d); Fig. 10 of RB shows the de-

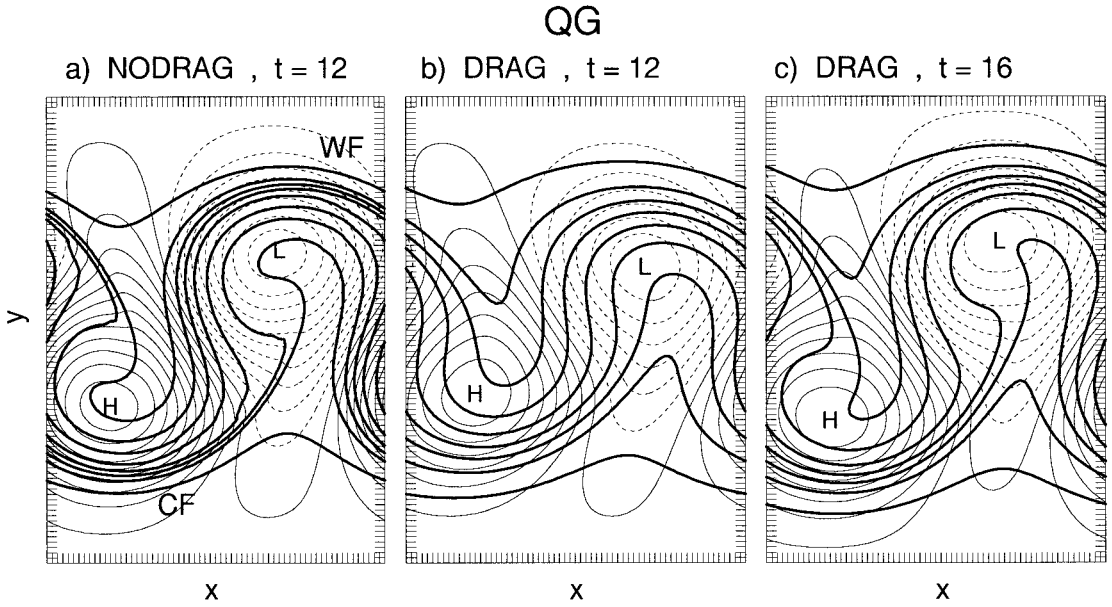

FIG. 3. Nondimensional surface potential temperature (heavy lines, contour interval = 0.3) and geopotential ϕ (thin lines, interval = 0.1) from a quasigeostrophic numerical simulation with (a) no surface drag, displayed at $t = 12$; (b) surface drag, displayed at the same time; and (c) surface drag, displayed at $t = 16$. Plotting conventions are as described in Fig. 1. The domain is 4 units in x and 5.532 in y; ticks indicate gridpoint locations.

velopment in dimensional units], the growing disturbance is basically the most unstable normal mode. As part of the nonlinear evolution, we observe in Fig. 3a a wrapping of the tongue of warm air into the low and an equivalent tongue of cold air around the high; on the periphery of these tongues there are strong θ gradients (the WF and the CF). Due to the symmetry of the problem, the WF and the CF are of equal size, shape, and intensity ($|\nabla\theta|$).

The effects of surface friction are accounted for in QG theory by considering the lower surface ($z = 0$) of the inviscid adiabatic interior flow to be at the top of a thin boundary layer through which there may be vertical motion (see Pedlosky 1987, section 6.6). For the standard Ekman boundary layer, the vertical velocity at the top of the boundary layer is related to the interior geostrophic vorticity through

$$w_\infty = \frac{E_V^{1/2}}{2\epsilon}(\partial_{xx}\phi + \partial_{yy}\phi) \tag{1}$$

[Pedlosky 1987, Eq. (6.6.8)], where E_V is the Ekman number and ϵ is the Rossby number. Using (1) in the prognostic equation for θ at $z = 0$ in the QG model with $E_V^{1/2}/2\epsilon = 0.1$,[2] we obtain the surface θ and pressure fields shown in Figs. 3b,c. As compared to the no-drag case, the case with drag shows that both the WF and CF are weaker at the same time after an identical initialization (Fig. 3b). This comparative weakness could be expected since drag decreases the growth rate of the unstable mode (Williams and Robinson 1974); however, integrating the drag case out to the time when $\phi'_{\max}$ is comparable to that in the no-drag case (Fig. 3c) still indicates weak fronts and little tendency for the warm (cold) tongue to wrap around the low (high), but rather to move more or less in the meridional direction throughout the integration.

Using standard QG scaling (see Pedlosky 1987, chap. 6), the nondimensional θ equation at the top of the boundary layer is

$$d_g\theta = -w_\infty, \tag{2}$$

where d_g is the time rate of change following the geostrophic motion. Since $-w_\infty \sim \phi$, Figs. 3b,c indicate that the progress of the warm tongue (say) on the level surface $z = 0$ is impeded by cooling at the tip of the tongue and that cooling in the warm tongue with respect to air farther north is frontolytical. A simple analytical argument can be made by recognizing that the smaller-scale motions that develop in the QG integrations can be described by

$$\phi = \phi_0 \exp(-|\mathbf{k}|z + i\mathbf{k}\cdot\mathbf{x}), \tag{3}$$

where $\mathbf{k}$ is the horizontal wavenumber vector. Substituting (3) into (1) allows (2) to take the form (in wavenumber space)

[2] For the parameters relevant to the PE simulations, $\epsilon \sim 0.7$, and thus the eddy viscosity implied by this choice is ~ 80 m^2 s^{-1}. Since the QG solutions grow more rapidly than the PE solutions, we conjecture that a larger viscosity is needed in the former for friction to have an effect comparable that observed in the latter. Be that as it may, a precise comparison between QG and PE models is not intended here.

$$d_g\theta = -\frac{E_V^{1/2}}{2\epsilon}|\mathbf{k}|\theta(|\mathbf{k}|), \tag{4}$$

since $\theta = \partial_z\phi$. Equation (4) shows that small-scale features, such as tongues and temperature gradients, are selectively damped by the Ekman effect.

In summary, surface drag weakens surface fronts in QG theory both through its cumulative effect on the baroclinic wave (e.g., decreased growth rates and altered synoptic-scale structure, as evidenced in Fig. 3) and through its instantaneous effect on frontogenesis as evidenced by the rhs of (4) (which represents frontolytical tilting of the basic-state static stability).

b. The θ budget in the PE simulations

Inherent in the approximations leading to (1) is the fact that θ within the Ekman layer is determined by the evolving value of θ at the bottom of the interior flow or, equivalently, the top of the Ekman layer (Pedlosky 1967, 475). In other words, in QG, $\theta(z = 0)$ evolves according to (2), which applies at the top of the Ekman layer, and as a consequence of the approximations leading to (1), $\theta(z = 0)$ is in effect instantaneously diffused through the Ekman layer. Hence, as far as QG theory is concerned, a surface front is a manifestation of a feature existing above the boundary layer. Motivated by this understanding of how surface drag works in QG theory, we present an analysis here of the PE θ field at $z = 500$ m, which is near the top of the Ekman layer δ ($\equiv\sqrt{2\nu/f} \approx 447$ m) in DRAG.

Figure 4 contains the θ budget corresponding to the time and location shown in Fig. 2a. The wave-relative flow $\mathbf{u}_{\text{rel}}$, vertical velocity w, and θ are displayed in Fig. 4a. (The budget is calculated relative to the wave so that time tendencies due to the wave propagation do not overwhelm those associated with frontogenesis.) In Fig. 4b, showing $-\mathbf{u}_{\text{rel}}\cdot\nabla\theta - w\partial_z\theta$, we observe that the cooling rate decreases rapidly toward the warm air in the vicinity of the incipient cold front; the corresponding decrease in the warming rate toward the cold air in the incipient warm front is much weaker. The separate contributions of horizontal and vertical advection are shown in Figs. 4c,d; these figures show that horizontal advection by itself would tend to produce equally strong cold and warm fronts; however, vertical advection strongly counters horizontal advection in the vicinity of the warm front. The similarity of the pattern of $-w\partial_z\theta$ to w suggests that the pattern of the former is simply a reflection of the pattern of the latter (cf. Fig. 4d with Fig. 4a). Perturbations in $\partial_z\theta$ (not shown) are also contributing in the same sense, since the ageostrophic boundary layer wind shear tends to decrease the static stability near CF and increase it near WF [for a discussion of a similar effect, see Bluestein (1993), 350–351]. Finally, vertical diffusion (not shown) is a small fraction of the advection terms at $z = 500$ m. Comparing w in Fig. 4a with ϕ in Fig. 2a indicates that the vertical motion is largely in phase with ϕ, as expected from the Ekman effect. We conclude that Ekman pumping is at root responsible for the lack of warm-air seclusion and a strong warm front in the DRAG case.

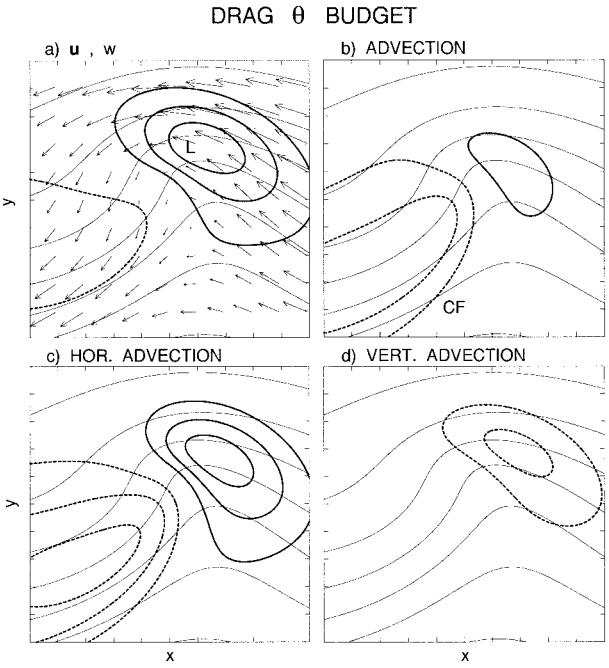

FIG. 4. Wave-relative θ budget on the 2000 × 2000 km subdomain indicated in Fig. 2a (DRAG, $t = 3.5$ d): (b) total advection, (c) horizontal advection, and (d) vertical advection (advection fields in heavy lines, interval = 0.5×10^{-4} K s^{-1}, zero lines not shown). Interpretation of the terms shown in (b)–(c) is aided by (a) wave-relative u (maximum vector length = 32.5 m s^{-1}) and vertical velocity w (contour interval = 0.005 m s^{-1}, zero line not shown). Tick marks indicate 200-km intervals. The θ field is shown in thin lines (c.i. = 5 K) in all panels. In (a) the L is slightly displaced from its position in Fig. 1a to avoid its being lost under the contour lines.

For comparison with the foregoing analysis of the DRAG case, we show in Fig. 5 the θ budget for the NODRAG case at $t = 2.5$ d and $z = 500$ m; horizontal advection (Fig. 5c) is the dominant contributor to the total (Fig. 5b), as vertical advection is weak (Fig. 5d). The distribution of warming and cooling implies that the warm tongue will wrap cyclonically around the low and that warm frontogenesis is stronger than cold frontogenesis. A fuller accounting of surface frontogenesis in the case without surface drag can be found in RSS.

In the case without surface drag the warm front tends to be produced near the pressure low, while the cold front forms between the low and the high. This asymmetry explains why Ekman pumping has a stronger effect on the warm front than on the cold front. But what explains the asymmetry in the inviscid model? The reasons for this, and more generally the asymmetry of the breaking pattern of the large-amplitude wave, is the subject of current research and is outside the scope of the present paper. Leaving aside the reasons for the behavior, we believe, based on our previous work (SSR), that

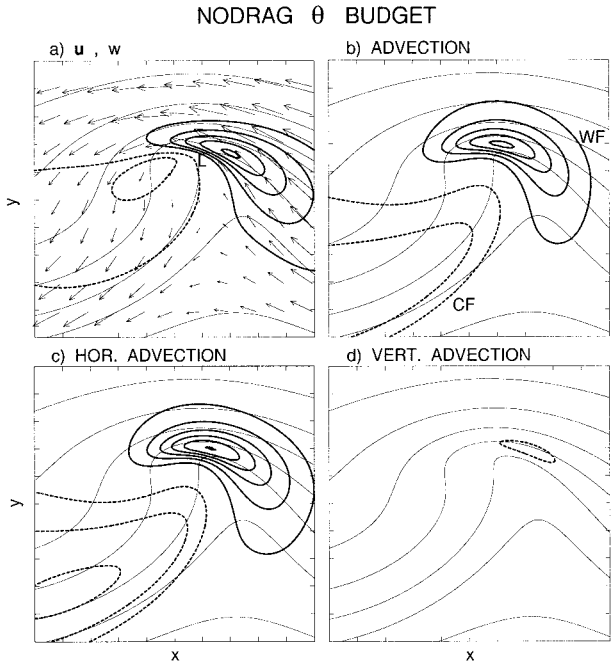

FIG. 5. As in Fig. 4, except for the 2000 × 2000 km subdomain indicated in Fig. 1a (NODRAG, $t = 2.5$ d).

there is an inherent tendency in the PE model for lows to be strong and narrow and highs to be weak and broad, and for the warm tongue to be wrapped cyclonically into the low, while the cold front extends in an arc between the high and the low. This basic behavior is seen in all published PE simulations (without drag) of baroclinic waves grown to large amplitude from the most unstable normal mode, including those done on a β-plane with meridional shear at the surface (Polavarapu and Peltier 1990) and those done on the sphere for a variety of different base states (Thorncroft et al. 1993; Hines and Mechoso 1993; Balasubramanian and Garner 1997).

c. Analysis of the cold front

As the baroclinic wave grows and fronts form, one expects that the QG-inspired diagnosis of the previous section will become less relevant. In the absence of a boundary layer, advection by the ageostrophic wind (due to thermal-wind imbalance) can enhance the geostrophic frontogenesis (Hoskins and Bretherton 1972). In the case with a boundary layer, θ at the bottom is no longer directly tied to θ at the top of the boundary layer, since ageostrophic boundary layer winds can play a role in advecting boundary layer θ (for a fuller discussion, see Snyder 1998). Therefore, in this section, we return to the more traditional analysis of frontogenesis in vertical cross sections extending from the ground to some distance above the top of the Ekman layer.

As a point of reference for the analysis of the CF in DRAG (Fig. 2), we first analyze the CF in NODRAG in a vertical cross section along the line indicated in Fig. 1c. Figure 6 shows the cross-front u, alongfront v, and vertical w components of wave-relative velocity along with the cross-front component of the geostrophic velocity u_g; the θ field is shown in every panel for reference. A quick estimate of the front-normal variation of u shows that it is about twice as large as that of u_g (consistent with analysis of the cold front made in Fig. 5d of RSS). All the cross sections taken together suggest the geostrophic–ageostrophic feedback of the Hoskins–Bretherton (1972) deformation model. However, note the appearance of vertically propagating gravity waves above the front (most evident in the w field; see Snyder et al. 1993).

Figure 7 contains the θ budget corresponding to the θ field in DRAG at $t = 5.5$ d (Fig. 2c). Overall, the conclusions from the earlier time (section 3b) are still supported; in particular, horizontal advection is still the main contributor to cold frontogenesis. One difference, however, is that the updraft at the leading edge of the cold front is now much more intense than previously (cf. Fig. 7a with Fig 4a), indicating more intense convergence at the cold front. In Fig. 8, we analyze the CF in a vertical cross section along the line indicated in Fig. 7d; the cross-front velocity indicates deformation in excess of the geostrophic value, as in the NODRAG case. However, it has long been suggested that convergence due to the Ekman-layer wind might also enhance frontogenesis (see the review in the introduction to Keyser and Anthes 1982).

To obtain an estimate of the Ekman-convergence effect in the present simulations, we compute

$$\overline{w}(z = \delta) = \frac{1}{2lf}[\tau_0^y(l) - \tau_0^y(-l)], \tag{5}$$

where τ_0^y is the alongfront surface stress and the overbar signifies an average in the cross-front direction over the distance $2l$. In the DRAG case, $\tau_0^y = Kv(z = 0)$; reading the numbers for $v(z = 0)$ from the box indicated in Fig. 8, (5) gives $\overline{w}(z = \delta) \approx (0.03 \text{ m s}^{-1})(3 \text{ m s}^{-1})/(50 \text{ km})/(10^{-4} \text{ s}^{-1}) \approx 0.018 \text{ m s}^{-1}$, which accounts for more than half the actual value seen in Fig. 8. Simulations with a more realistic boundary layer representation show an even stronger effect (see below). In spite of the stronger updraft, vertical advection of θ remains small since, as described above and evidenced in the u field of Fig. 8, the ageostrophic vertical wind shear in the vicinity of CF tends to weaken $|\partial_z\theta|$ in the boundary layer.

Based on the foregoing analysis, we conclude that a portion of the cold frontogenesis in DRAG is dynamically similar to that in NODRAG in that horizontal advection is primarily responsible (vertical advection, or the ''tilting'' effect, plays no important role) for frontogenesis and in that there appears to be a geostrophic–ageostrophic feedback along the lines of the Hoskins–Bretherton model. However, the present analysis shows that in DRAG, Ekman-layer-induced convergence is also an important contributor to frontogenesis.

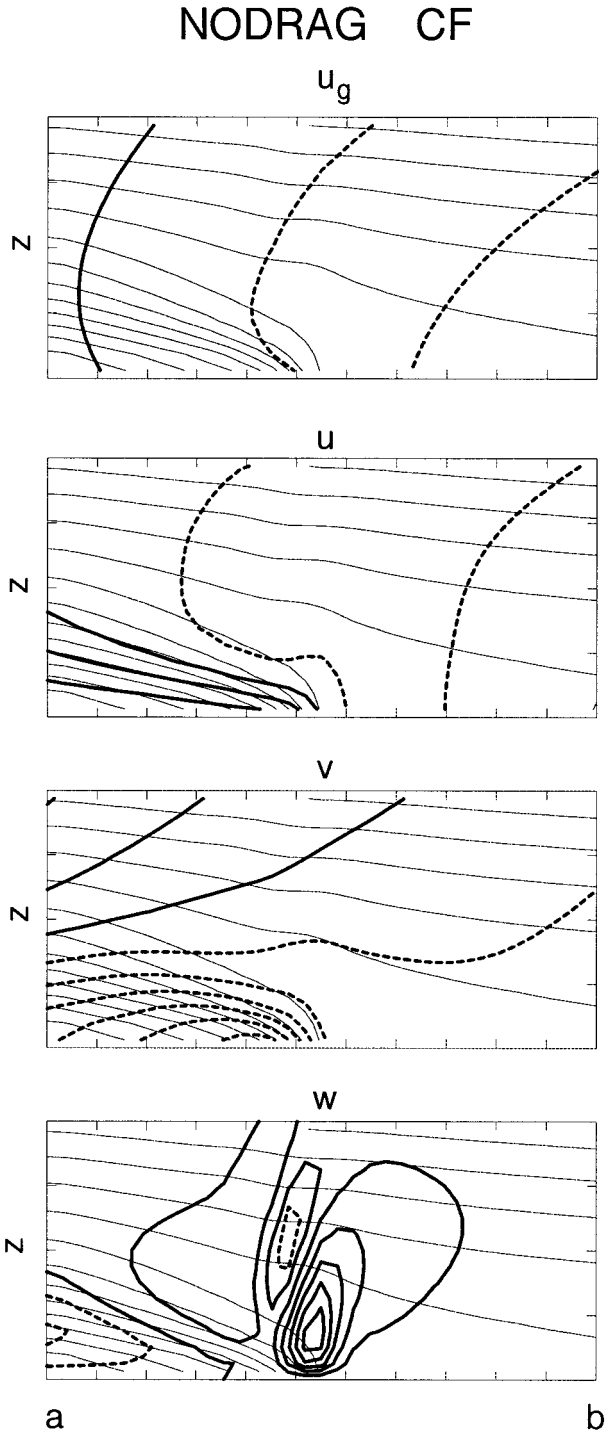

FIG. 6. Analysis of the cold front in the NODRAG case (along section a–b in Fig. 1c) through a vertical cross section showing wave-relative cross-front geostrophic velocity (u_g), cross-front velocity (u), alongfront velocity (v), and vertical velocity (w). The velocities are indicated by the heavy lines (horizontal components with contour interval = 4 m s^{-1}; vertical component contour interval = 0.01 m s^{-1} for $w > 0$ and interval = 0.005 m s^{-1} for $w < 0$; zero line is the first solid contour). The θ field is shown in thin lines (interval = 2 K) in all panels. The tick marks denote 1-km intervals in the vertical and ~50-km intervals in the horizontal.

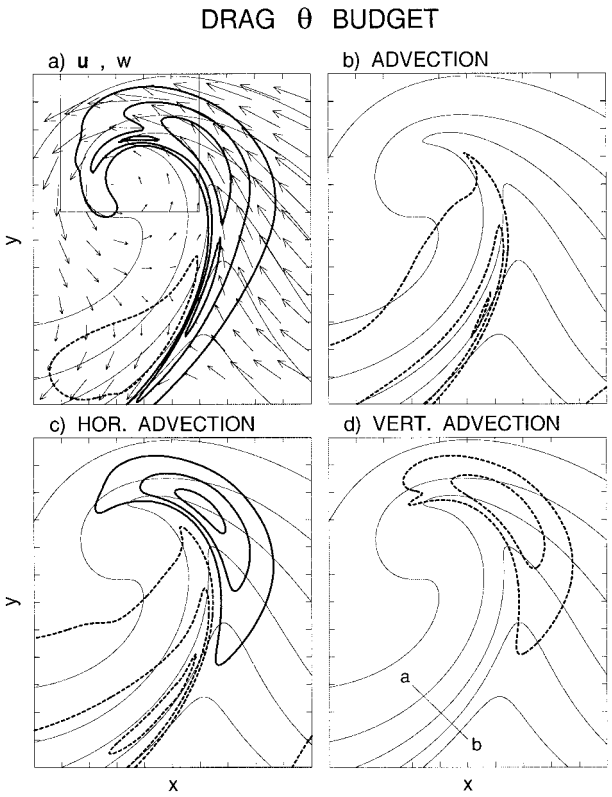

FIG. 7. As in Fig. 4, except at t = 5.5 d; the 2000 × 2400 km analysis subdomain is indicated in Fig. 2c. The box in Fig. 7a is the analysis domain for the DRAG part of Fig. 9.

As stated above, the present simulations indicate no important role in cold frontogenesis for vertical advection (tilting). This conclusion remains valid even in a simulation (described below) with a more realistic boundary layer representation. The absence of the tilting effect is consistent with Blumen (1980, p. 75) but in contrast to the result of Thompson and Williams (1997, see their Fig. 14). Given the overall similarity of the latter numerical results to the present ones, we think that the difference must reside in the different lower boundary condition used on surface θ. With fixed surface temperature, warm advection ahead of the cold front is over a colder surface; hence, a strong stable layer is created and, subsequently, may be tilted by the frontal updraft. In the present DRAG run, on the other hand, the lower boundary condition $\theta_z = 0$ means that stability should be tending toward zero in the boundary layer, and hence tilting would not contribute to frontogenesis.

d. The vertical velocity field near the cyclone center

It has long been appreciated by meteorologists that Ekman pumping has an important effect on the distribution of clouds and precipitation in the vicinity of the cyclone center (see, e.g., Carlson 1991, section 9.1).

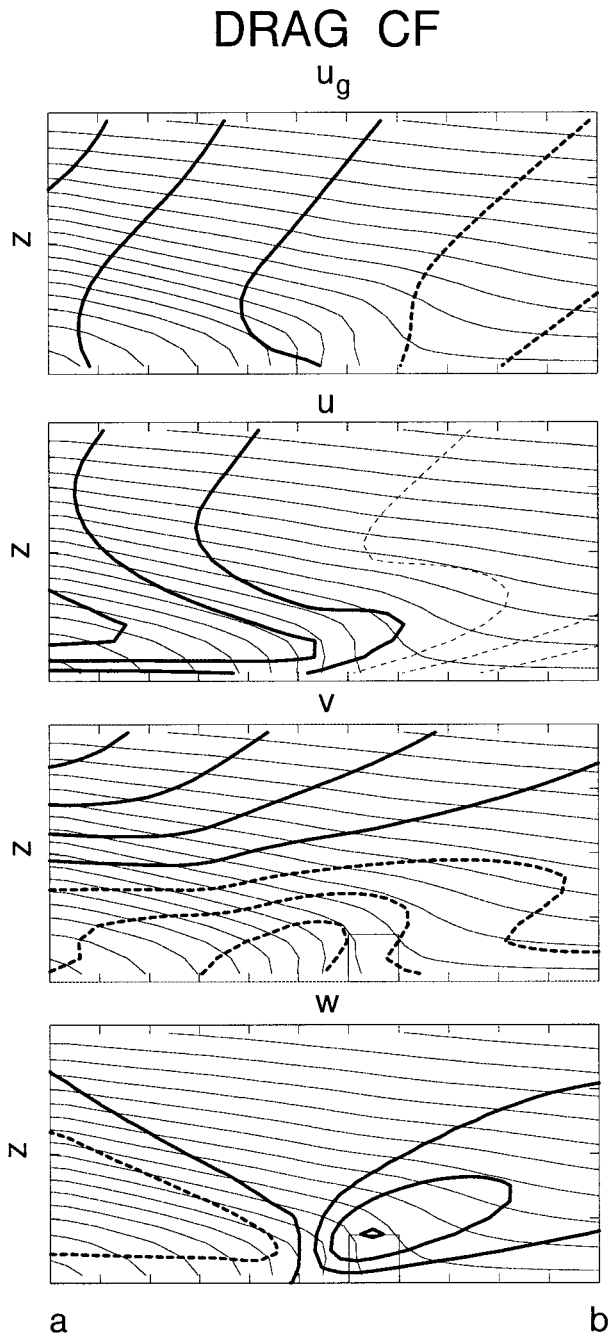

FIG. 8. As in Fig. 6, except for the section indicated in Fig. 7d (DRAG), and for w, contour interval = 0.01 m s^{-1}.

Without surface drag, the rising and sinking motion near the surface is nearly $\pi/2$ out of phase with the surface pressure wave for the two-dimensional Eady wave (see Fig. 13.4 of Gill 1982); including an Ekman layer in the form of (1) forces the vertical motion at the top of the boundary layer to be nearly in phase with surface pressure wave (see Fig. 7 of Williams and Robinson 1974). Comparing w and ϕ in NODRAG (Figs. 5a and 1a) with the same fields in DRAG (Figs. 4a and 2a) shows this effect.

At later times in DRAG, a small-scale intense updraft located near the tip of the warm tongue appears (Fig. 7a); this was initially a matter of some concern, given the ever-present possibility of spurious numerical results on small scales. Through resolution tests, we are convinced that the feature is part of the genuine solution to the governing equations. At later times in DRAG, there is a localized increase of $|\nabla\theta|$ on the north side of the warm tongue; at first glance, one might think that the small-scale feature in w is a manifestation of a localized frontal circulation. Figure 9 presents a close-up view of w and ground-relative **u** from NODRAG and DRAG within the boxes indicated in Figs. 1b and 2c, respectively. The top row of Fig. 9 shows that $w \approx 0$ at the pressure minimum in NODRAG but that, in DRAG, the smaller-scale feature in w is nearly coincident with the pressure low. The vertical cross sections through the updraft in NODRAG indicate that the vertical motion is on the warm-air side of the warm front but not at the maximum in the θ field; the circulation in the plane of the cross section is deep and closely associated with $\nabla\theta$ (for a more precise description pertaining to the case at hand, see RSS's Fig. 10 and accompanying discussion). The vertical cross section through the updraft in DRAG shows, in contrast, that the updraft is right at the center of the warm tongue and limited vertically such that the maximum is near the Ekman-layer depth; the cross-front velocity component indicates convergence restricted to the boundary layer, while the alongfront component suggests a vertically localized vortex. The updraft magnitude is consistent with that estimated from (5).

The foregoing evidence leads us to believe that the small-scale feature in the w field is peculiar to the DRAG case. As the warm tongue narrows, so does the corresponding pressure field [recall that with (3), $\phi \sim -\theta$] the Ekman flow in the boundary layer therefore begins to respond to a more localized interior geostrophic vorticity distribution. It is interesting to speculate further that, in a moist atmosphere, the low-level updraft combined with weak stability aloft would produce strong cumulus convection at the center of the pressure low.

e. Simulations with a more realistic boundary layer model

The extreme simplicity of the boundary layer model used in the DRAG case requires us to check that the conclusions drawn from the DRAG–NODRAG comparison would survive if a more realistic boundary layer model were used. To that end, the case designated PBL uses the scheme of Troen and Mahrt (1986; only the neutral case is considered, since surface heat flux is set to zero) to compute an eddy viscosity,

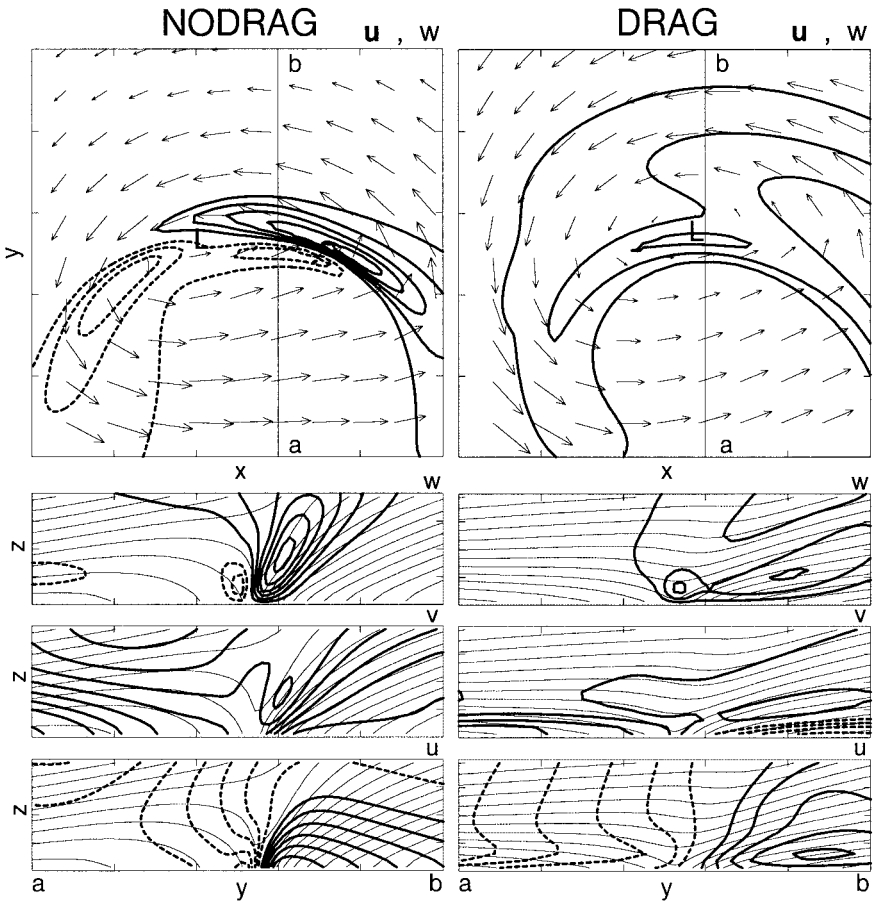

FIG. 9. Comparison of w at $z = 500$ m between NODRAG (left column, analysis domain indicated in Fig. 1b) and DRAG (analysis domain indicated in the smaller box of Fig. 2c). Top row shows x–y plot of w (interval = 0.01 m s^{-1}), and ground-relative velocity vectors (maximum vector length $\approx$ 35 m s^{-1}). The vertical cross sections arranged in the columns beneath the respective horizontal plots show (in heavy lines) w (interval = 0.02 m s^{-1} in NODRAG, interval = 0.01 m s^{-1} in DRAG), the (approximately front normal) y velocity v (interval = 2 m s^{-1}), and the (approximately front parallel) x velocity u (interval = 5 m s^{-1}), together with the θ field (thin lines, interval = 2 K). Zero lines are not plotted for any of the fields. The tick marks denote 1-km intervals in the vertical and 200-km intervals in the horizontal.

$$\nu = \max\left[\nu_b,\ u_* kz\left(1 - \frac{z}{z_{\mathrm{BL}}}\right)^p\right],$$

where $\nu_b = 2.5$ m^2 s^{-1} is a background value, $k = 0.4$ is von Kármán's constant, and $p = 2$ in this study. The friction velocity,

$$u_* = c_D^{1/2}(u^2 + v^2)|_{z=\Delta z/2},$$

where $c_D = k^2/\ln(\Delta z/2z_0)$; with $\Delta z = 250$ m and $z_0 = 10$ cm, $c_D \approx 0.0033$. The boundary layer height z_{BL} is the maximum height for which the bulk Richardson number is less than a critical value; that is, $z_{\mathrm{BL}}(x, y)$ satisfies

$$\frac{gz_{\mathrm{BL}}[\theta(z_{\mathrm{BL}}) - \theta(z = 0)]}{\theta_0[u^2(z_{\mathrm{BL}}) + v^2(z_{\mathrm{BL}})]} = \mathrm{Ri}_c,$$

where g is the acceleration due to gravity and $\theta_0 = 300$ K is a reference temperature; we take $\mathrm{Ri}_c = 0.1$.

In PBL, the wave develops more quickly since the larger viscosity is applied selectively and a nonlinear drag law is used by the boundary layer model. Figure 10 shows the PBL θ budget at a mature phase of wave development. The qualitative similarity of the θ field to that shown in Fig. 7 indicates that the conclusions drawn from DRAG carry over to the more realistic PBL case. More specifically, Fig. 10 indicates that Ekman-pumping-associated vertical advection counters horizontal advection so that the WF is weaker than the CF and that horizontal advection is the major player in cold frontogenesis. The small-scale feature in the w field near the cyclone center also survives. Vertical cross sections through the cold front (Fig. 11) indicate geostrophic–ageostrophic feedback with a strong contribution from Ekman convergence; with $\tau_0^y = c_D(\sqrt{u^2 + v^2}\,v)_{z=\Delta z/2}$ and the relevant values of (u, v) from the box shown in Fig. 11, (5) indicates that $\overline{w}(z = 1000\ \mathrm{m}) \approx$

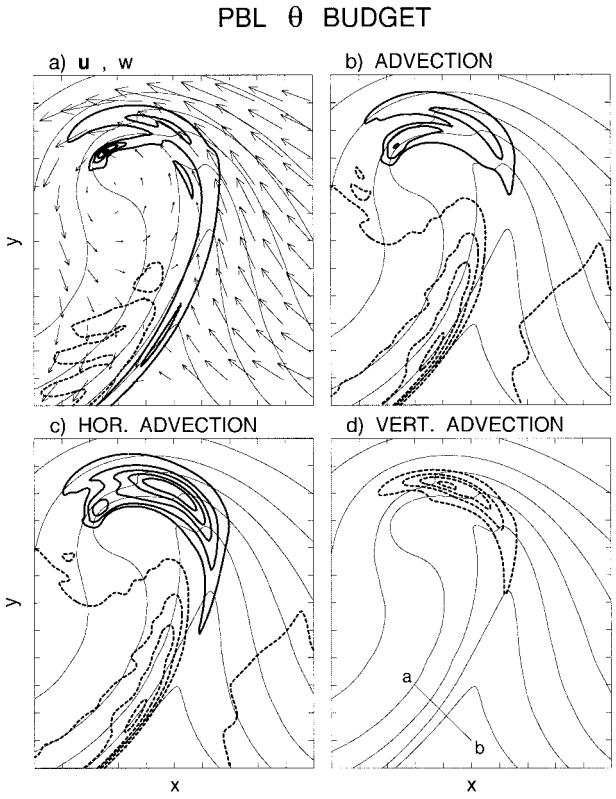

FIG. 10. As in Fig. 4, except for the PBL case, and the advection contour interval = $\times 10^{-4}$ K.

$(0.0033)[(12\ \text{m s}^{-1})^2 - (8\ \text{m s}^{-1})^2]/(50\ \text{km})/(10^{-4}\ \text{s}^{-1}) \approx 0.05\ \text{m s}^{-1}$, which accounts for most of the actual value seen in Fig. 11.

4. Summary

The present results are summarized in the schematic diagrams shown in Fig. 12. Without surface drag (Fig. 12a), our analysis here and in a previous paper (RSS) shows that the fronts form through geostrophic forcing with ageostrophic feedback, along the lines of the Hoskins–Bretherton (1972) model. The difference between the warm front and cold front is related to the inherent asymmetry introduced by nongeostrophic effects (SSR). A ubiquitous feature of that asymmetry is that the warm front extends through to the center of the low, while the cold front extends in an arc between the (relatively weaker) high and the low. With the addition of drag (Fig. 12b), the cooling due to Ekman pumping, being roughly proportional to the low pressure perturbation, acts to prevent the warm tongue from progressing toward the cold air and is thus frontolytical. The cold front, positioned between the high and the low, where Ekman pumping is weak, is therefore relatively unaffected. Moreover, since the high is weaker than the low, the warming due to Ekman suction is relatively weaker in the cold-air tongue.

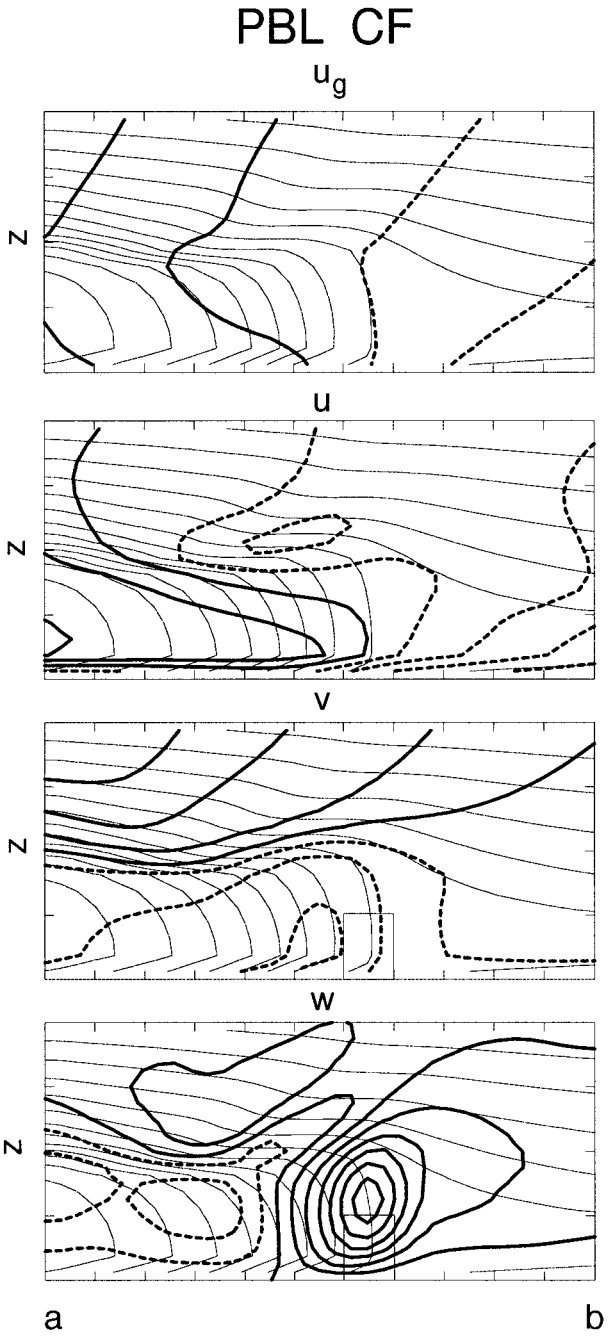

FIG. 11. As in Fig. 6, except for the section indicated in Fig. 10d.

The cold front in either case is ultimately due to differential advection of cold air toward warm. In the case with drag, a significant portion of the ageostrophic response is due to Ekman convergence on the cyclonic-shear side of the alongfront jet. We suspect that while the horizontal resolution is high with respect to previous studies of this type, it may not be high enough to capture the full importance of the Ekman effect (e.g., Snyder and Keyser 1996).

The strong updraft at the tip of the warm tongue, near

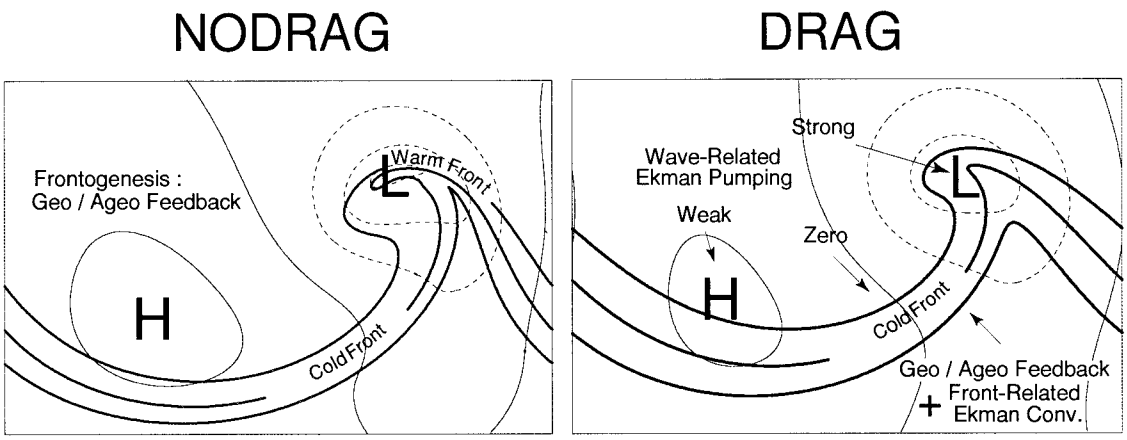

FIG. 12. Schematic diagram summarizing results.

the location lowest surface pressure, appears to be driven by Ekman-layer dynamics on a scale much smaller than that of the parent baroclinic wave.

One final caveat is that studies such as the present one should be considered as building blocks to be used when trying to comprehend a necessarily more complex reality. The effects of moisture, for example, are known to be produce important modifications of cold-frontal structure (Orlanski et al. 1985). It remains to be seen how moisture affects the different responses of the warm front and the cold front to surface drag found using dry models.

Acknowledgments. Conversations during the course of this work with H. Bluestein and D. Keyser are gratefully acknowledged.

REFERENCES

Balasubramanian, G., and S. T. Garner, 1997: The role of momentum fluxes in shaping the life cycle of a baroclinic wave. *J. Atmos. Sci.,* **54,** 510–533.

Bannon, P. R., and T. L. Salem, 1995: Aspects of the baroclinic boundary layer. *J. Atmos. Sci.,* **52,** 574–596.

Bluestein, H. B., 1993: *Synoptic-Dynamic Meteorology in Midlatitudes.* Vol. II. Oxford University Press, 594 pp.

Blumen, W., 1980: A comparison between the Hoskins–Bretherton model of frontogenesis and the analysis of an intense surface frontal zone. *J. Atmos. Sci.,* **37,** 64–77.

Carlson, T. N., 1991: *Mid-Latitude Weather Systems.* Harper Collins Academic, 507 pp.

Gill, A. E., 1982: *Atmosphere-Ocean Dynamics.* Academic Press, 662 pp.

Hines, K. M., and C. R. Mechoso, 1993: Influence of surface drag on the evolution of fronts. *Mon. Wea. Rev.,* **121,** 1152–1175.

Hoskins, B. J., and F. P. Bretherton, 1972: Atmospheric frontogenesis models: Mathematical formulation and solution. *J. Atmos. Sci.,* **29,** 11–37.

Keyser, D., and R. A. Anthes, 1982: The influence of planetary boundary layer physics on frontal structure in the Hoskins–Bretherton model. *J. Atmos. Sci.,* **39,** 1783–1802.

Kuo, Y.-H., and S. Low-Nam, 1994: Effects of surface friction on the thermal structure of an extratropical cyclone. *Proc. Int. Symp. on the Life Cycles of Extratropical Cyclones,* Vol. II, Bergen, Norway, University of Bergen, 129–134.

Orlanski, I., B. Ross, L. Polinsky, and R. Shaginaw, 1985: Advances in the theory of atmospheric fronts. *Advances in Geophysics,* Vol. 28B, Academic Press, 223–252.

Pedlosky, J., 1967: The spin up of a stratified fluid. *J. Fluid Mech.,* **28,** 463–479.

——, 1987: *Geophysical Fluid Dynamics.* Springer-Verlag, 624 pp.

Polavarapu, S. M., and W. R. Peltier, 1990: The structure and nonlinear evolution of synoptic-scale cyclones: Life cycle simulations with a cloud-scale model. *J. Atmos. Sci.,* **47,** 2645–2672.

Rotunno, R., and J.-W. Bao, 1996: A case study of cyclogenesis using a model hierarchy. *Mon. Wea. Rev.,* **124,** 1051–1066.

——, W. C. Skamarock, and C. Snyder, 1994: An analysis of frontogenesis in numerical simulations of baroclinic waves. *J. Atmos. Sci.,* **51,** 3373–3398.

Snyder, C., 1998: Approximate dynamical equations for fronts modified by the planetary boundary layer. *J. Atmos. Sci.,* **55,** 777–787.

——, and D. Keyser, 1996: The coupling of fronts and the boundary layer. Preprints, *Seventh Conf. on Mesoscale Processes,* Reading, United Kingdom, Amer. Meteor. Soc., 520–522.

——, W. C. Skamarock, and R. Rotunno, 1991: A comparison of primitive-equation and semigeostrophic simulations of baroclinic waves. *J. Atmos. Sci.,* **48,** 2179–2194.

——, ——, and ——, 1993: Frontal dynamics near and following frontal collapse. *J. Atmos. Sci.,* **50,** 3194–3212.

Thompson, W. T., and R. T. Williams, 1997: Numerical simulations of maritime frontogenesis. *J. Atmos. Sci.,* **54,** 314–331.

Thorncroft, C. D., B. J. Hoskins, and M. E. McIntyre, 1993: Two paradigms of baroclinic-wave life-cycle behavior. *Quart. J. Roy. Meteor. Soc.,* **119,** 17–55.

Troen, I., and L. Mahrt, 1986: A simple model of the atmospheric boundary layer; sensitivity to surface evaporation. *Bound.-Layer Meteor.,* **37,** 129–148.

Williams, G. P., and J. B. Robinson, 1974: Generalized Eady waves with Ekman pumping. *J. Atmos. Sci.,* **31,** 1768–1776.